

The Impact of the Geometry of Cellular Structure Made of Glass-Filled Polyamide on the Energy-Absorbing Properties of Design Elements

Semen V. Diachenko^{1,2,*} – Sergey V. Balabanov¹ – Maxim M. Sychov^{1,2} –
German E. Litosov² – Nikita V. Kiryanov²

¹ Russian Academy of Sciences, Institute of Silicate Chemistry, Russia

² Saint Petersburg State Institute of Technology, Russia

Energy-absorbing properties of cellular materials with D, G, IWP, N, P, Q, PJ triply minimal energy surface geometries were investigated. Materials were made of glass-filled polyamide by selective laser sintering. Mechanical properties of cellular structures were determined depending on the geometry: the highest specific compressive strength $\sigma_{sp,max} > 8 \text{ MPa}\cdot\text{cm}^3/\text{g}$ is possessed by samples with the geometry IWP* and PJ; the highest specific energy absorption $A_{sp} = 14.5 \text{ MJ}/\text{m}^3$ is in the sample with the geometry N. A mass-strength criterion for cellular structures is proposed. The maximal values of mass-strength criterion are from samples with geometries N, IWP* and PJ; 4.16 MPa²/g, 3.51 MPa²/g, and 2.88 MPa²/g. The adequacy of applying the Gibson-Ashby equation for fabricated cellular materials with triply periodic minimal surfaces (TPMS) geometry has been proven.*

Keywords: additive technologies, selective laser sintering, polyamide, glass, triply periodic minimal surface, energy absorption, dampers.

Highlights

- Using selective laser sintering additive manufacturing and glass-filled polyamide material, cellular materials with the geometry of triply minimal energy surfaces possessing high mechanical properties were developed.
- The paper proposes a mass-strength criterion for assessing cellular structures. The maximal mass-strength criterion values are from samples with geometries N, IWP* and PJ; 4.16 MPa²/g, 3.51 MPa²/g, and 2.88 MPa²/g.
- It is shown that Gibson-Ashby equation holds for the developed cellular materials dependence of relative compressive strength on relative density.

0 INTRODUCTION

Cellular materials have a wide range of applications in many sectors of mechanical engineering, in engineering and scientific tasks [1] and [2]. In particular, such materials can effectively dissipate various types of energy: acoustic [3], thermal [4], and mechanical energy [5] and [6], for example in the space industry, where they are used as dampers and energy absorbers in landing devices. It is known that one of the responsible stages of a space mission is the landing of a spacecraft. To minimize the risks of breaking the spacecraft during landing, you can use design elements made of lightweight cellular energy-absorbing materials, which changes the mass-dimensional characteristics of the spacecraft, and reduces the load on the landing device. Materials with high porosity and large plastic deformations are used as energy absorbers for landing devices: foams, honeycombs, thin-walled crushable shells, rods made of plastic steel [7] to [9]. Due to their cellular structure, such materials have unusual mechanical properties. They can be quite rigid, but at the same time light, and when deformed under the action of external forces, they are able to absorb more energy.

Thanks to innovations in the field of three dimensional (3D) printing, it has become possible to manufacture cellular materials of complex shape. Some of them, such as wood and bone, are found in nature [10], while others, such as polymer foams or cellular structures, are man-made. However, these structures are either doubly periodic (cellular structures), and therefore have anisotropy of properties, or have only a near order, are irregular in space, for example, due to the uneven distribution of pores (polymer or metal foams).

In the works of academician Shevchenko et al. [11] and [12], it has been shown that to improve the physical and mechanical properties of cellular materials used in mechanical engineering, it is promising to use materials with the geometry of triply periodic minimal surfaces. Triply periodic minimal surfaces (TPMS) are regular structures with periodicity along three axes and zero mean curvature [13]. They have a strict mathematical equation that allows variation of the periodicity parameters, and therefore, the properties of the resulting materials [14] to [18]. However, until recently, the fabrication of such cellular structures was hindered by technical limitations. Only through the development of additive manufacturing technologies

(a key element of Industry 4.0) has it become possible to create and investigate complex geometric cellular structures, including those with TPMS geometry. One of the key features of Industry 4.0 is the use of smart manufacturing technologies, which facilitates precise control over the geometric characteristics and physical properties of such cellular designs [19]. Of particular interest are the mechanical properties of materials with TPMS geometry, it is known that such materials have high mechanical properties [20] and [21]. Like other porous structures, TPMS can also be used as effective energy absorbers during compression [22]. Due to the combination of high porosity, strength and smoothness of the surface, such materials are used in medicine, for example as implants [23].

This study examines the physical and mechanical properties of products with topologies based on TPMS. Seven different geometries with a constant parameter value of $t = 0$ were considered. The specimens were manufactured using selective laser sintering (SLS) from glass-filled polymer powder. The main mechanical properties of cubic cellular structures were analyzed, also a critical comparison of their energy absorption properties was conducted, aiming for potential applications in structural components.

1 METHODS

1.1 Manufacturing Technology

Digital models of cellular structure samples were generated using parametric modeling in the 'RhinoCeros 5' software with the 'Grasshopper' plugin.

The sample fabrication technology is based on the method of SLS, which involves layer-by-layer formation of parts through the interaction of a laser with a polymer powder composition, melting the surface layers of the particles. The choice of this manufacturing technology is due to the fact that selective laser sintering allows for the production of the highest quality and most durable products in large volumes. It is evident that for the implementation and widespread use of structures with TPMS geometry, it is necessary to use the most widely adopted materials and technologies in the industry. Therefore, in this work, 3D printing was conducted on the serial equipment 'Farsoon SS/HT 403P', using a polymer glass-filled powder based on polyamide grade 'FS3401GB' produced by 'Farsoon'. The use of glass-filled polyamide is justified by its high physical and mechanical properties, while being less expensive compared to carbon-filled and even unfilled

polyamide. Preliminary selection of technological parameters of the process was carried out, based on the complexity of digital models of products, which were set by the control program of the 3D printer. As a result, the main parameters of the technological process were determined, presented in Table 1.

Table 1. Parameters of 3D Printing

No.	Parameter	Value
1	Fill laser power, P [W]	85
2	Layer thickness, h [μm]	119
3	Fill distance, s [μm]	300
4	Laser scan speed, V [m/s]	15.2
5	Energy density, E [J/cm^3]	157

The energy density E is calculated according to Eq. (1):

$$E = \frac{P}{Vhs}. \quad (1)$$

During three dimensional (3D) printing, 7 varieties of cellular structures in the form of a cube with a side size of 30 mm and a wall thickness of 0.8 mm were fabricated. Each type of structure was manufactured in a series of 5 samples to improve the reliability of the experiments. In addition, witness samples were fabricated for various tests (compression, bending, etc.) to determine the basic properties of the material used.

After the main stage of 3D printing, post-processing of the products was carried out. Cleaning with compressed air, including manual cleaning, of excess unsintered powder and residues in the channels of elements on the 'FS04-PPS Cleaning Station' equipment. Then, final cleaning from powder residues and processing of products to reduce surface roughness with glass spherical shot 0.4 mm, ..., 0.6 mm on the '110/130-I-M Shot Blasting Chamber' equipment.

1.2 Method of Analysis

To study the structure and morphology of the surface, as well as the elemental composition of the initial powder, a scanning electron microscope (SEM) 'Tescan Mira 3 LMH' with an attachment for micro X-ray spectral (MXRS) analysis 'Aztec Ultum MAX 100' was used. The distribution of particles by powder size was carried out using the laser particle analyzer 'Shimadzu SALD Nano - 7500' in a solution of isopropyl alcohol, as well as the properties of the powder using the 'Bettersizer Powder Pro A1' setup.

The analysis of the chemical structure was carried out on the IR-Fourier spectrometer 'Shimadzu IR Tracer-100' with the single- reflection ATR 'Specac' attachment. The range of infrared (IR) spectrum shooting is $\tilde{\nu} = (4000, \dots, 350) \text{ cm}^{-1}$, resolution 4 cm^{-1} , accumulation of spectra 32. Thermal analysis of polyamide was carried out on the differential scanning calorimeter 'Shimadzu DSC-60 Plus'. Experiment conditions: reference is Al_2O_3 (10 mg); heating rate $20 \text{ }^\circ\text{C}/\text{min}$; atmosphere argon. Tensile tests, three-point bending, and compression of test samples were conducted in accordance with GOST 11262-2017 [24], GOST 4648-2014 [25], GOST 4651-2014 [26] on the 'Shimadzu AG-X Plus' testing machine with a crosshead speed of $10 \text{ mm}/\text{min}$. Compression tests were conducted on the 'IR 5143-200-11' testing machine with a crosshead speed of $5 \text{ mm}/\text{min}$. The determination of the coefficient of linear thermal expansion (CLTE) was carried out on the thermomechanical analyzer 'Shimadzu TMA-60' in accordance with GOST 15173-70 in the temperature range from $20 \text{ }^\circ\text{C}$ to $100 \text{ }^\circ\text{C}$. Hardness tests of test samples were conducted by the Shore method in accordance with GOST 24621-2015 on the 'TVR-D' durometer. Roughness parameters were determined

in accordance with GOST 2789-73 on the 'ISHP-210' profilometer. Measurement of geometric parameters of samples before and after testing was carried out with a caliper 'SHC-1-150-0.01'.

2 RESULTS AND DISCUSSION

2.1 Polymer Powder Study

Based on the results of SEM analysis of the initial powder polymer composition PA-12 of the 'FS3401GB' brand, from which cellular structures with geometry were made, it can be concluded that the granules of the composition are conglomerates of predominantly spherical shape (Figs. 1 to 4). The polymer composition is filled with glass of shard shape with linear dimensions from $10 \text{ }\mu\text{m}$ to $70 \text{ }\mu\text{m}$; and glass microspheres, from $1 \text{ }\mu\text{m}$ to $50 \text{ }\mu\text{m}$.

Using the back-scattered electron (BSE) detector, areas of the powder composition filled with spheres and shard-shaped material (gray local area) and polymer (black local area) were identified, Fig. 5.

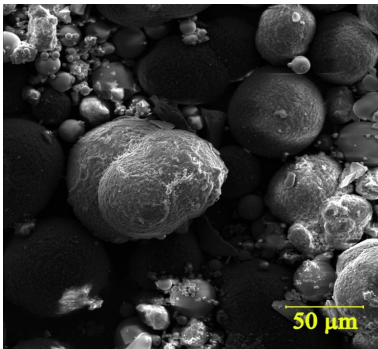


Fig. 1. General view of polymer powder granules

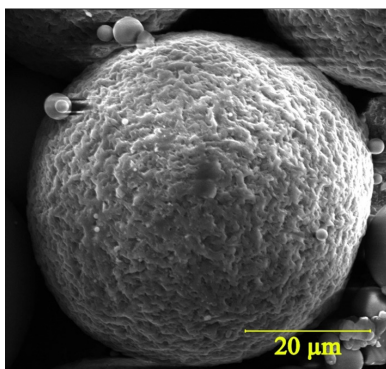


Fig. 2. Morphology of a polymer granule

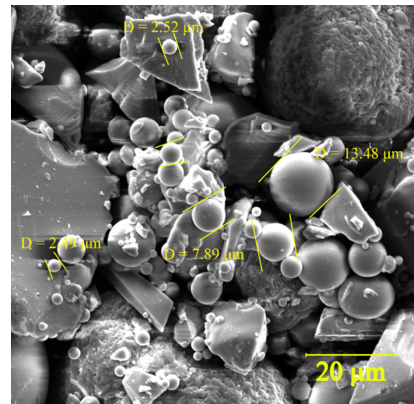


Fig. 3. Sizes of microspheres in the powder composition

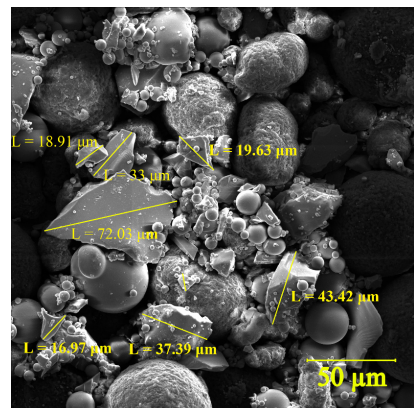


Fig. 4. Size of chopped glass fiber in the powder composition

According to the elemental analysis - spheres and parts of shard shape have an identical composition, which corresponds to glass based on silicon oxide with additions of Na, Mg, Ca oxides (Table 2, Spectrum 1 and 2). The 'Spectrum 3' mark corresponds to the spherical polymer matrix made of polyamide.

Table 2. Elemental composition of particles

Spectrum No.	C	Na	O	Al	Si	Mg	Ca	K
Spectrum 1	10.2	7.0	42.0	0.3	31.9	2.2	6.2	0.1
Spectrum 2	8.2	6.6	42.2	0.3	40.0	2.4	8.2	0.4
Spectrum 3	89.1	-	10.9	-	-	-	-	-

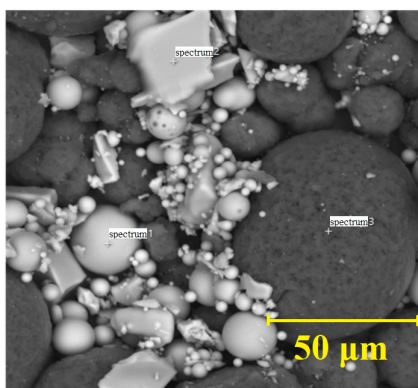


Fig. 5. Morphology of the polymer and filler in BSE mode

The distribution of particles by size in the powder sample was carried out using the laser diffraction method, the granulometric composition is shown in Table 3. In addition, the bulk density of the powder was determined to be 0.64 g/cm³, the density after shaking was 0.77 g/cm³, and the compressibility of the powder was 17 %.

Table 3. Indicators of the dispersity of the polymer powder

Parameter	D10	D50	D90
Value [μm]	17.7	39.7	78.7

Fig. 6 shows the IR-Fourier spectrum of the sample of the provided material. The analysis of the characteristic peaks is given in Table 4.

According to the data obtained using infrared Fourier spectroscopy, it can be concluded that this sample, according to its chemical structure, is a polyamide 12 and contains amide and methyl groups [27]. According to the literature, the crystalline phase of this polymer is in the alpha form [28].

According to the thermal analysis of polyamide the glass transition temperature (T_g) was determined according to [29], and the melting temperature (T_m) was determined according to [30]. The results are

presented in Table 5 and Fig. 7, where 1 is a glass transition zone, and 2 a melting zone.

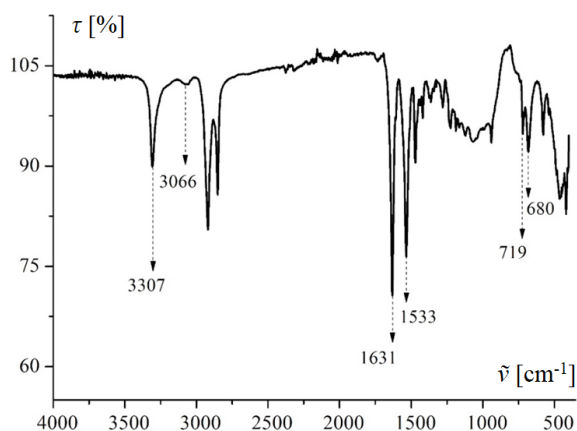


Fig. 6. IR-Fourier spectra of the polymer

Table 4. The ratio of the wave number to the functional groups of the polymer

No.	Wave number $\tilde{\nu}$, [cm ⁻¹]	Attribution of bands to functional groups
1	3307	N-H (secondary amine)
2	3066	Amide II (N-H)
3	2918, 2850	CH ₂ , VH ₃ – asymmetrical valence oscillations
4	1631	Amide II (C = O-NH-)
5	1533	Deformation oscillations -NH- (Amide II)
6	1471, 1419	Deformation oscillations CH ₂
7	1361	Torsional oscillations CH ₂
8	1120	Valence C-C
9	719, 680	Pendulum-NH oscillations

Table 5. Thermal and relaxation effects of the polymer sample

Parameter	T_g	T_m
Value, [°C]	51.9	186.2

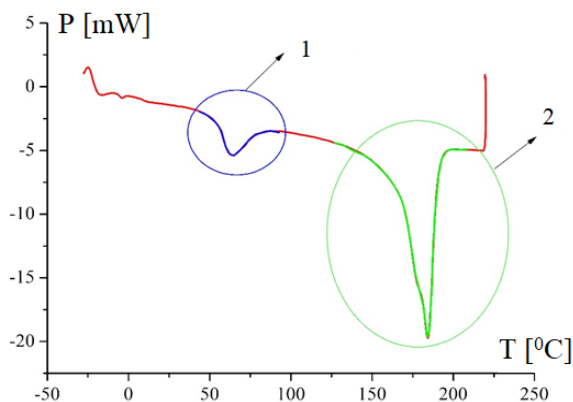


Fig. 7. Thermogram of the polymer material sample

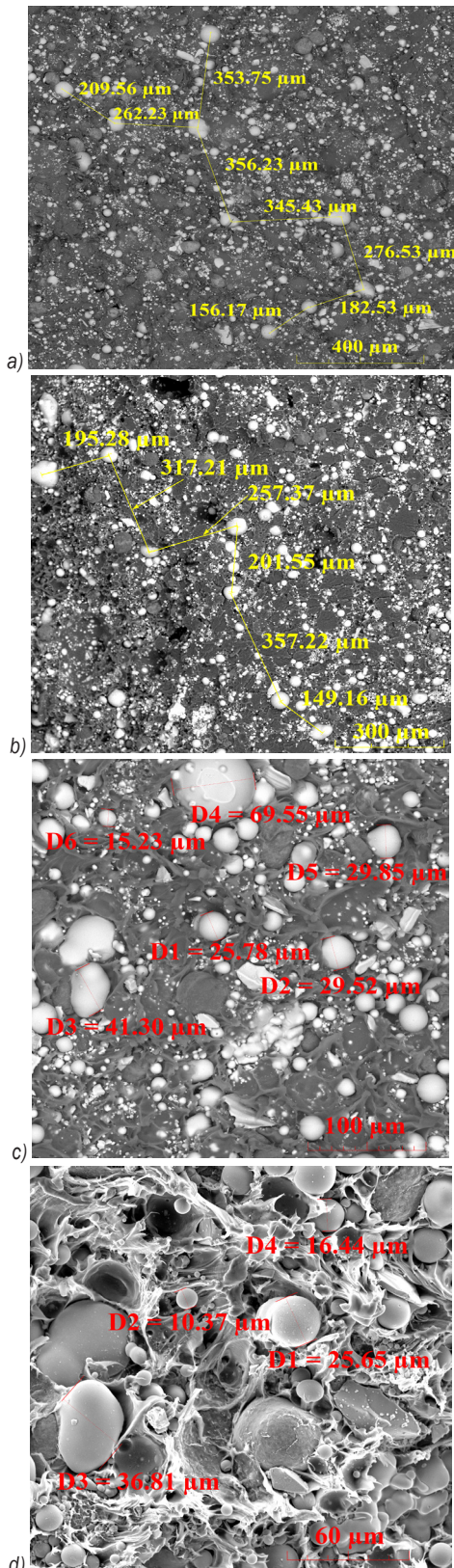


Fig. 8. Micrographs of a cross-section of polymer material after sintering made at different magnifications

Based on Table 5, it can be concluded that the polymer is predominantly in the amorphous phase, which is why a high glass transition temperature is observed compared to industrial polyamide 12 (PA 12), according to [31] from 30 to 40°C. The crystallinity percentage is 31 % [32]. The melting temperature corresponds satisfactorily to the certificate for this material 184 °C.

2.2 Investigation of Polymer Structure and Properties

Upon analyzing Fig. 8, a cross-section of the manufactured 3D polyamide sample, it can be noted that the fracture surface is characterized by a large

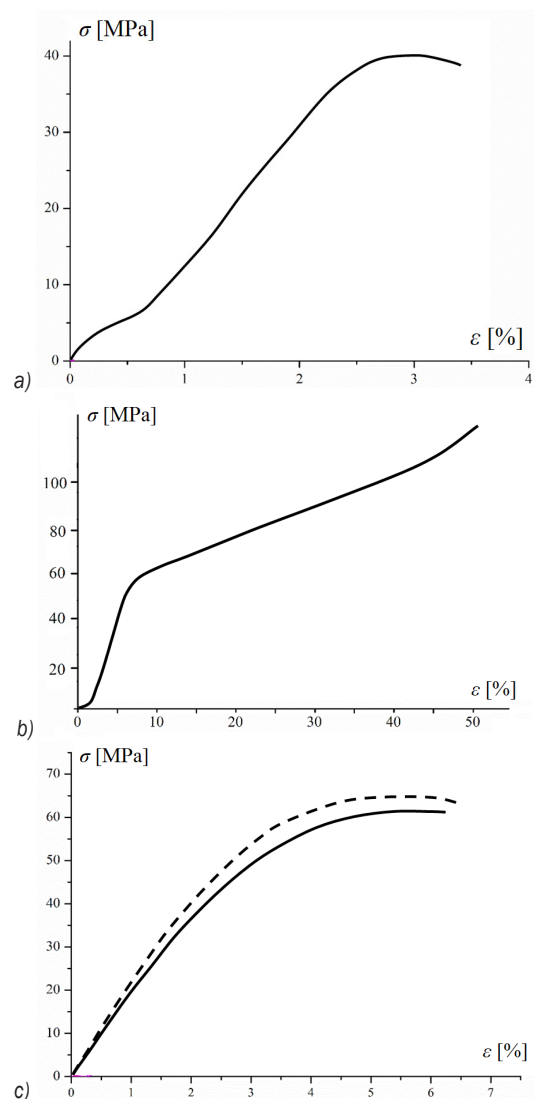


Fig. 9. Deformation curves of polyamide material in various types of tests: a) tension, b) compression, and c) bending (solid line: II; dotted line: ⊥)

number of brittle fracture foci along the boundaries of the glass filler, which likely indicates the relatively high hardness of the samples and the low plasticity of the material. The majority of the glass phase is found in the form of spheres of various sizes, confirmed both by the particles (white local areas in BSE images) and by a large number of craters. Despite this, a small number of glass particles and fragmentary form are also observed. The low content of non-spherical glass in the sample compared to the original powder may be associated with their dense distribution in the polymer matrix. The size of the spherical glass varies from 0.5 μm to 80.0 μm , and around each particle, a polymer shell is observed, as can be seen from the images in the semi-dark areas (light gray local spherical areas). To analyze the uniformity of the distribution of glass particles on the sample surface, the average distance between the largest spherical particles ($L \geq 50 \mu\text{m}$) was measured, as smaller particles are distributed non-segregated among them. Based on the measurement results, it can be concluded that the range of linear distance values between large particles varies from 150 μm to 350 μm , with an average value of approximately 250 μm .

Analysis of the physical and mechanical properties of 3D witness samples was carried out according to three main types of tests for polymer products: tension, compression and three-point bending (Fig. 9). The obtained physical and mechanical properties are consistent with the certificates for this material and are similar when testing materials produced

by the pressure casting method [32]. The results of mechanical characteristics, as well as other properties of the material 'FS3401GB', are presented in Table 6.

2.3 Investigation of the Mechanical Properties of Cellular Samples

Cellular samples with various geometries were manufactured by 3D printing at a constant value of the parameter $t = 0$ (where t is the level of the isosurface). The equations from [37] and [38] were used to create 3D models of macroporous samples. The approximating equations of the TPMS and TPMS-similar surfaces and their general form are presented in Table 7.

To investigate the influence of geometry at a constant parameter t on the physical and mechanical properties of cellular samples, deformation curves were obtained during the compression of samples (dependence of stress on relative deformation). All tests were conducted with the samples positioned along the construction axis, similar to the application of such samples as energy absorbers. The initial data and test results are shown in Figs. 10 and 11 and Tables 8 and 9 [39].

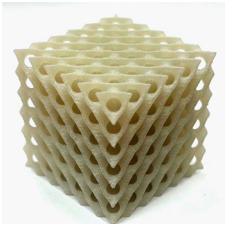
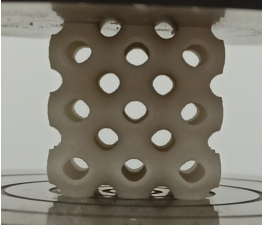
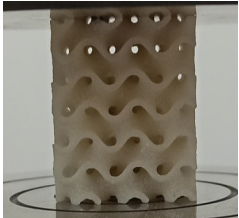
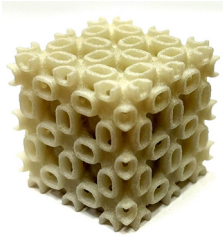
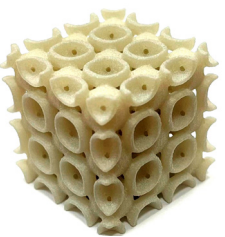
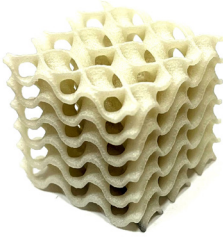
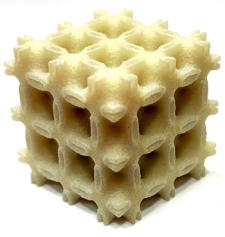
Based on the form of the deformation curves of the samples (Fig. 10), it can be concluded that TPMS samples with different geometries predominantly correspond to the plastic material and have compression diagrams similar to that of cellular

Table 6. Properties of samples manufactured under the given 3D printing regime

No.	Test Type	Property	Value
1	Tensile tests (+)	Tensile strength [MPa]	39
		Relative elongation [%]	3.5
		Tensile modulus of elasticity [MPa]	1496
2	Bending tests (II)	Bending strength at failure [MPa]	61
		Bending modulus of elasticity [MPa]	2008
3	Bending tests (+)	Bending strength at failure [MPa]	65
		Bending modulus of elasticity [MPa]	2235
4	Compression tests (II)	Compressive strength at failure [MPa]	61
		Compressive modulus of elasticity [MPa]	1030
		Relative deformation [%]	8.0
5	Hardness (II)	Hardness (ball indentation [33]) [MPa]	153
		Elasticity [%]	82
		Plasticity [%]	18
		Shore method type D [34]	69 (D/1:69)
6	Determination of CLTE (II) [35]	$\beta \cdot 10^6$ [K ⁻¹] (in the range 20 °C, ..., 100 °C)	106
7	Roughness parameter [36]	Ra [μm]	6.0
8	Determination of density	ρ [g/cm ³]	1.26

* II tests parallel to the printing axis of the sample; + test perpendicular to the printing axis of the sample

Table 7. Cellular structures of TPMS with various geometries

No.	Type of surface, equation	General view	No	Type of surface, equation	General view
1	Diamond (D-surface, Diamond): $\sin(x) \cdot \sin(y) \cdot \sin(z)$ $+ \sin(x) \cdot \cos(y) \cdot \cos(z)$ $+ \cos(x) \cdot \sin(y) \cdot \cos(z)$ $+ \cos(x) \cdot \cos(y) \cdot \cos(z) = 0$		5	Primitive (P-surface, Schwarz primitive): $\cos(x) + \cos(y)$ $+ \cos(z) = 0$	
2	Gyroid (G-surface, Gyroid): $\cos(x) \cdot \sin(y) + \cos(y) \cdot \sin(z)$ $+ \cos(z) \cdot \sin(x) = 0$		6	PJ – surface $\cos(x) + \cos(y) + \cos(z)$ $+ 4\cos(x)\cos(y)\cos(z) = 0$	
3	IWP* (IWP similar): $\cos(x)\cos(y) + \cos(y)\cos(z)$ $+ \cos(z)\cos(x) = 0$		7	Q – surface: $(\cos(x) - 2\cos(y)) \cdot \cos(z)$ $- \sqrt{3} \cdot \sin(z) \cdot (\cos(x-y) - \cos(x))$ $+ \cos(x-y) \cdot \cos(z) = 0$	
4	Nevius (N-surface, Nevius surface): $3 \cdot (\cos(x) + \cos(y) + \cos(z))$ $+ 4 \cdot (\cos(x) \cdot \cos(y) \cdot \cos(z)) = 0$				

structures. As an example, the deformation curve (Fig. 11) of a sample with D geometry is considered, which, like cellular materials, has an area of elastic deformation (initial area under the curve, marked in Fig. 11, zone A), elastic-plastic deformation (zone B) and plastic deformation (area of sharp load increase, zone C).

In zone A, a linear increase in stress is noted with an increase in relative deformation, which corresponds to the law of elasticity, based on which, the Young's modulus E for this sample can be determined. After the transition from elastic to elasto-plastic deformation, a typical non-linear dependence of stress

on deformation is observed until the sample's strength limit σ_{max} (temporary resistance) is reached. From Fig. 11 it follows that after passing the maximum, there is a decrease in stress with an increase in deformation (relaxation), and then an increase in stress and the passage of several peaks of unequal height and shape, not exceeding the strength limit. These fluctuations can be associated with the destruction of individual layers of cells. It should be noted that during the tests, samples with P geometry also showed the properties of a brittle material, which was noted in a sharp decrease in stress after the area of elastic deformation up to the destruction of the sample. The limit value

of deformation (ϵ_{max}) for the studied samples did not exceed $\epsilon_{max} \approx 65\%$. After this boundary the area of sharp load increase begins, and the structure ceases to work as an effective energy absorber. For the use of samples as mechanical energy absorbers, naturally, zones A and B are important.

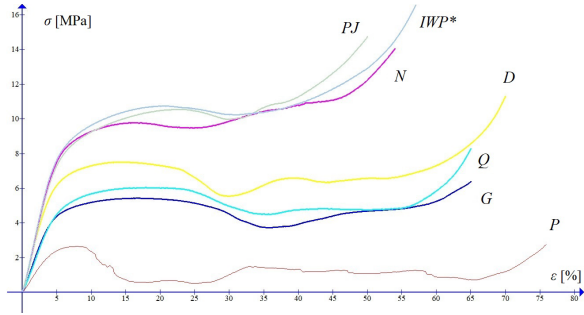


Fig. 10. Deformation curves of compression samples with TPMS geometry

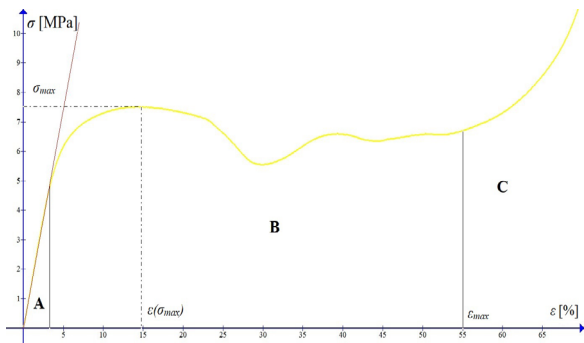


Fig. 11. Deformation curve of compression sample with D geometry

Based on the compressive strength σ_{max} , all samples may be conditionally divided into categories:

low-strength (P), medium-strength (D, G, Q) and high-strength (N, PJ, IWP^*) geometries. Moreover, for all curves, it can be noted that the higher the σ_{max} , the lower the deformation value ϵ_{max} , which is probably non-linearly related to the degree of TPMS volume filling. A similar trend is for the value of $\epsilon(\sigma_{max})$ the value of deformation at the strength limit.

Table 8. Initial geometric parameters of cellular structures

No.	Sample code	V [cm ³]	S_s [cm ²]	S_b [cm ²]	φ [%]	α [%]
1	D	8.14	213.5	3.21	30.1	35.7
2	G	6.61	174.1	2.02	24.5	22.4
3	IWP*	7.51	197.7	1.68	27.8	18.7
4	N	7.48	195.7	1.71	27.7	19.0
5	P	5.04	132.1	1.12	18.7	12.4
6	PJ	8.25	219.0	2.16	30.6	24.0
7	Q	7.70	207.1	2.31	28.5	25.7

where V is volume, S_s surface area, S_b base area, φ degree of volume filling, and α degree of base filling

For each geometry, you can calculate the damping characteristic, the energy of load (impact) absorption A at different sections of the deformation curve (integral area):

$$A = \int_0^{\epsilon} \sigma d\epsilon. \tag{2}$$

The value of A can be calculated at different sections of the deformation curve, for example, up to the strength limit, denoted as A_1 , over the entire section (up to densification), A_3 ; and up to the minimum value of deformation among all sample geometries, at which densification occurs, A_2 . Note that for the PJ sample, A_3 is slightly lower than the others ($\epsilon_{max} = 32\%$), so

Table 9. Test results of various cellular structures

No.	Sample	Parameter values						
		σ_{max} [MPa]	$\sigma_{sp,max}$ [MPa·cm ³ /g]	$\epsilon(\sigma_{max})$ [%]	ϵ_{max} [%]	A_1 [MJ/m ³]	A_2 [MJ/m ³]	A_3 [MJ/m ³]
1	D	7.52	5.97	14.8	55.0	0.88	2.03	3.51
2	G	5.43	4.31	16.3	58.9	0.71	1.50	2.68
3	IWP*	10.8	8.57	20.6	33.3	1.75	2.95	3.08
4	N	9.78	7.76	16.4	43.8	1.25	2.76	4.01
5	P	2.65	2.10	8.3	65.2	0.16	0.39	0.78
6	PJ	10.50	8.33	23.1	32.0	1.94	2.85	2.85
7	Q	6.04	4.80	18.0	55.0	0.86	1.64	2.38

where σ_{max} is compressive strength, obtained by calculating the overall base area ($S \approx 9 \text{ cm}^2$), $\sigma_{sp,max}$ specific compressive strength, referred to the material density, $\epsilon(\sigma_{max})$ and ϵ_{max} are relative deformation to the strength limit and to densification, A_1 load absorption energy at ϵ_{max} (to the strength limit), A_2 load absorption energy at ϵ_{max} (as for the PJ surface), and A_3 load absorption energy at ϵ_{max} over the entire area (to densification).

it is correct to compare all samples at this value. For the use of cellular materials as energy absorbers, it is necessary to strive for the maximum value of A_3 , i.e. so that the sum of the areas of zones A and B is the largest. The results of calculating the values of A_i are given in Table 9.

Highlighting the maximum values of energy absorption, it can be noted that the largest value of A_1 belongs to the *PJ* geometry, A_2 *IWP**, and A_3 *N*. All these geometries belong to the high-strength category. However, based on the data in Tables 8 and 9, it is still necessary to take into account the degree of volume filling of the cellular structure. Fig. 12 shows a histogram for all geometries, where the height is taken as the value of A_{sp} , specific energy absorption (per unit of material distributed in the volume in accordance with the geometry; $A_{sp} = A_3/\varphi$).

From Fig. 12 it follows that the *N* geometry has the maximum value of specific energy absorption, but due to the lower degree of filling, the medium-strength category of *G* and *D* geometries has identical and superior values to the high *PJ* and *IWP**. The obtained result can have a strong influence at the stage of choosing the TPMS geometry when designing structures, since, all other things being equal, a lower degree of filling will give an advantage in mass-dimensional characteristics.

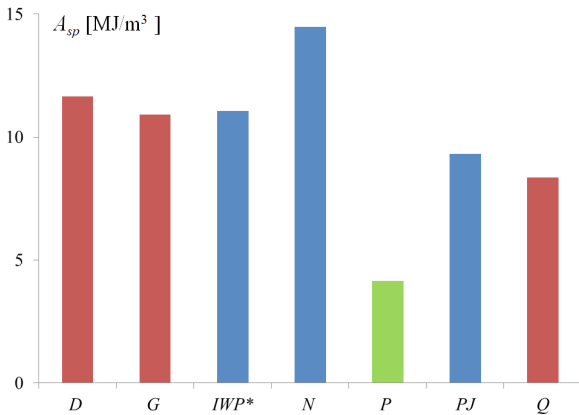


Fig. 12. Histogram of specific energy absorption values for different TPMS geometries: blue is high-strength, red medium-strength, and green low-strength

Table 9 shows the values of the compressive strength σ_{max} , based on the calculation of the applied force to the overall area of the samples. However, if we calculate the strength of the samples only on the area of the base filled with material S_b (Table 8), taking into account that the area of the samples in height changes no more than 5 %, then the values of

σ_{max} will have a significant difference compared to the original values. Comparative data are given in Table 10. In addition, it is possible to compare the masses of m cellular structures and introduce a mass-strength criterion taking into account the energy absorption capacity A_3 of the cellular structure in accordance with Eq. (3):

$$K = \frac{\sigma_{max} \cdot A_3}{m} \tag{3}$$

Based on Table 10, it can be noted that the structures *N* and *IWP** have the highest value of the *K* criterion.

Table 10. Strength and mass-strength criterion of various TPMS geometries

No.	Sample code	σ_{max} [MPa]	σ'_{max} [MPa]	m [g]	K [MPa ² /g]
1	<i>D</i>	7.52	21.08	10.3	2.57
2	<i>G</i>	5.43	24.19	8.3	1.74
3	<i>IWP*</i>	10.80	57.86	9.5	3.51
4	<i>N</i>	9.78	51.47	9.4	4.16
5	<i>P</i>	2.65	21.29	6.4	0.32
6	<i>PJ</i>	10.50	43.75	10.4	2.88
7	<i>Q</i>	6.04	23.53	9.7	1.48

2.4 Analysis of the Compliance with the Gibson-Ashby Equation for the Investigated Cellular Structures

The mechanical behavior of cellular materials depends on a multitude of factors, ranging from the properties of the base material to the geometry of the cell and the degree of volume filling. The study [40] states that the strength of cellular materials follow the relationship:

$$M = C\rho^n, \tag{4}$$

where M is the normalized mechanical property, C is a geometric parameter that depends on the applied load, morphology, boundary conditions, and manufacturing defects. This equation was experimentally derived from a large amount of empirical data and is known as the Gibson-Ashby equation. The behavior of cellular materials corresponds quite accurately to this pattern. Depending on the properties of the cellular material (degree of filling, material used, shape of the cells), the value of the parameter C can vary from 0.1 to 4.0, and the change in the exponent n is usually within the range of 1.5 to 3.5.

By applying Eq. (4) to calculate the values of the Young's modulus and the strength limit of cellular materials, we can obtain Eqs. (5) and (6) for the Gibson-Ashby equation:

$$\frac{E}{E_s} = C \left(\frac{\rho}{\rho_s} \right)^n, \quad (5)$$

where E is the Young's modulus of the cellular material, E_s is the Young's modulus of the base solid material, ρ is the density of the cellular material, and ρ_s is the density of the base solid material.

$$\frac{\sigma}{\sigma_s} = C \left(\frac{\rho}{\rho_s} \right)^n, \quad (6)$$

where σ is the strength of the cellular material, and σ_s is the strength of the base solid material.

Based on the results of compression tests of cellular materials with TPMS geometry, a dependency of the relative strength (σ/σ_s) on the relative density (ρ/ρ_s), essentially the material volume filling ϕ , can be constructed. The dependency is presented in Fig. 13.

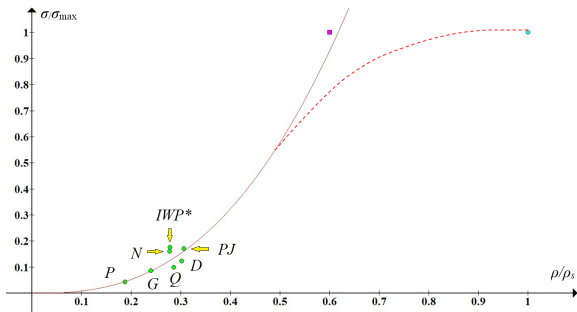


Fig. 13. The dependence of the relative strength (σ/σ_s) on the relative density (ρ/ρ_s) for different geometries of cellular structure

Based on the results shown in Fig. 13, the experimental data can indeed be described by a power-law relationship, similar to the Gibson-Ashby law, if the cellular structures are made of glass-filled polyamide. In this case, the equation takes the following form:

$$\frac{\sigma}{\sigma_s} = 3.5 \times \left(\frac{\rho}{\rho_s} \right)^{2.6}. \quad (7)$$

From this, the desired coefficients for the given material are respectively $C = 3.5$ and $n = 2.6$. In their studies, scientists have indicated that the Gibson-Ashby law adequately describes the behavior of cellular materials with a power law dependency for fillings less than 0.8, and in some cases, less than 0.6. This is likely because at high relative densities, the material may exhibit solid-like properties with spherical voids [40]. Using the described thesis for this dependency according to Eq. (7), it can be noted that the limiting value of the filling fraction $\rho/\rho_s \approx 0.6$

(indicated by a different color point) represents the strength limit of the material, i.e. $\sigma \approx \sigma_s$. However, in reality, this is likely unattainable because porous materials will not be stronger than monolithic materials. Therefore, the probable endpoint of the real curve is indicated by a dashed line.

Using the obtained empirical Eq. (7) and the Young's modulus of the material (3D glass-filled polyamide) under compression from Table 6, denoted as E_s , the values of the strength limit σ (where $\sigma = \sigma_{max}$) and Young's modulus E for some geometries of cellular materials are calculated and compared with experimental data. The comparison results are presented in Table 11. From the table, it can be seen that the experimental and calculated data have a slight discrepancy, which confirms the adequacy of the curve approximation according to Eq. (7).

Table 11. Comparison of physical and mechanical properties of cellular materials obtained experimentally and by calculation

No.	Sample	Filling degree (ϕ)	Property	Experiment	Calculation
1	G	0.245	Compressive strength	5.43	5.51
			σ_{max} [MPa]		
2	D	0.301	Young's modulus	152.1	158.9
			E , [MPa]		

3 CONCLUSIONS

As a result of the work carried out, seven different geometries of cellular materials were developed, manufactured, and studied: D , G , IWP^* (IWP -similar), N , P , Q , PJ surfaces. The samples were made from glass-filled polyamide 12 using selective laser sintering on the 'Farsoon SS/HT 403P' 3D printer. During the work, the main properties of the 3D material 'FS3401GB' were studied, which showed a positive result for use in the manufacture of structures with cellular material geometry. However, to increase the strength properties of the material, it is recommended to use glass particles exclusively in the form of spheres with a size distribution corresponding to the distribution of pores in the polyamide matrix for their subsequent filling.

Cellular materials from the high-strength category of geometries have the highest strength limit $\sigma_{max} = 10.8$ MPa, namely: the cellular material sample with IWP^* geometry; the highest specific energy absorption $A_{sp} = 14.5$ MJ/m³ a sample with N geometry. However, for the design of energy-

absorbing structures, for example, for aerospace vehicles or high-speed bolides, in addition to the A_3 value, mass-dimensional characteristics are also important. Therefore, along with the N geometry, when other things being equal, D and G geometries may be of interest when calculating dampers, despite the higher strength limit at IWP^* , as these samples have a lower degree of volume filling. In addition, high-strength geometries, which include IWP^* , have a smaller value of the ultimate deformation ε_{\max} , which is important when changing the size of the structure under external influence.

Samples with the low-strength P geometry exhibit the highest ultimate deformation (ε_{\max}). However, due to their low ultimate compressive strength, their applicability in this kind is unlikely. Therefore, a strengthening modification is required, although, other things being equal, the mass of this geometry is minimal. When introducing the mass-strength criterion K , taking into account the energy absorption capacity, it is possible to identify a structure with a geometry N , which has a value of $K = 4.16 \text{ MPa}^2/\text{g}$, which correlates with the results of comparing samples by specific energy absorption A_{sp} . Therefore, it can be concluded that the cellular structure surface N has the best energy-absorbing properties of all the studied samples.

Main conclusions of the work:

1. Lightweight cellular materials (a wall thickness of about 0.8 mm) with high values of specific strength and energy absorption were developed using triple periodic minimal surfaces geometry, glass filled polyamide material and selective laser sintering (energy density $E = 157 \text{ J/cm}^3$) industrial additive manufacturing, providing a step toward practical implementation of mechanical metamaterials.
2. An inversely proportional relationship has been identified between the values of the compressive strength σ_{\max} and the ultimate deformation ε_{\max} of the studied cellular structures with the geometry of periodic cellular materials, regardless of the degree of volume filling φ .
3. Criteria for the selection of periodic cellular materials have been proposed based on the main mechanical properties: strength limit σ_{\max} , ultimate deformation ε_{\max} , specific energy absorption of the load A_{sp} , and the mass-strength criterion K , taking into account the energy absorption capacity. Among the studied samples the highest specific strength belongs to geometries IWP^* , PJ and N ($8.6 \text{ MPa} \cdot \text{cm}^3/\text{g}$, $8.3 \text{ MPa} \cdot \text{cm}^3/\text{g}$ and $7.8 \text{ MPa} \cdot \text{cm}^3/\text{g}$). As a result,

the maximal energy absorption values are from samples with geometries N , D and IWP^* (4.0 MJ/m^3 , 3.5 MJ/m^3 and 3.1 MJ/m^3 accordingly). The maximal mass-strength criterion values are from samples with geometries N , IWP^* and PJ ($4.16 \text{ MPa}^2/\text{g}$, $3.51 \text{ MPa}^2/\text{g}$, and $2.88 \text{ MPa}^2/\text{g}$).

4. For the manufactured samples with the geometry of periodic cellular materials, the Gibson-Ashby equation for cellular double-periodic structures is adequately applicable when studying the dependence of specific strength on the degree of filling.

4 ACKNOWLEDGEMENTS

This work was carried out within the framework of the RSF project No. 20-73-10171 "Next-generation energy-absorbing materials based on gradient cellular structures".

5 REFERENCES

- [1] Feng, J., Fu, J., Yao, X., He, Y. (2022). Triply periodic minimal surface (TPMS) porous structures: from multi-scale design, precise additive manufacturing to multidisciplinary applications. *International Journal of Extreme Manufacturing*, vol. 4, 022001, DOI:10.1088/2631-7990/ac5be6.
- [2] Yeo, S.J., Oh, M.J., Yoo, P.J. (2019) Lightweight materials: Structurally controlled cellular architectures for high-performance ultra-lightweight materials. *Advanced Materials*, vol. 31, no. 34, DOI:10.1002/adma.201970245.
- [3] Yang, W., An, J., Chua, C.K., Zhou, K. (2020) Acoustic absorptions of multifunctional polymeric cellular structures based on triply periodic minimal surfaces fabricated by stereolithography. *Virtual and Physical Prototyping*, vol. 15, no. 2, p.242-249, DOI:10.1080/17452759.2020.1740747.
- [4] Surendra, S.R., Balkrishna, M., Pradeep K., Mohammad, A. (2023). *Flow Characterization in Triply-Periodic-Minimal-Surface (TPMS) based Porous Geometries: Part 2 - Heat Transfer*, p. 1-31, DOI:10.21203/rs.3.rs-2427715/v1.
- [5] Gibson, L.J., Ashby, M.F. (1997). Chapter 8 - Energy absorption in cellular material. *Cellular Solids Structure and Properties*, 2nd ed. Cambridge University Press, Cambridge, p. 309-344, DOI:10.1017/CB09781139878326.010.
- [6] DeValk, T., Lakes, R. (2021). Poisson's ratio and modulus of gyroid lattices. *Physica Status Solidi B*, vol. 258, 2100081, DOI:10.1002/pssb.202100081.
- [7] Rabinovich B.A. (2014). *Crew Safety During Landing Impact of a Descent Vehicle Against Hard Soil*. Moscow, (in Russian)
- [8] Aleshin, V.F., Kolobov, A.Yu., Makarov, V.P., Petrov Yu.A. (2010). Spacecraft landing devices based on foams and honeycomb blocks. *Nauka and Obrazovanie*, No. 4, 1. (in Russian)
- [9] Markov, V.A., Pusev, V.I., Selivanov, V.V. (2012). Issues of application of highly porous metals and cellular structures for protection against shock wave loads. *Voprosy oboronnoy tekhniki*, no. 7-8, 54. (in Russian).

- [10] Kovalev, I. (2005) Butterflies and helicopters. *Bulletin of the Entomological Society of Canada*, vol. 37, no. 3, p. 140-142.
- [11] Shevchenko, V.Ya., Sychev, M.M., Lapshin, A.E., Lebedev, L.A. (2018). Ceramic materials with the topology of triple periodic minimal surfaces for constructions functioning under conditions of extreme loads. *Glass Physics and Chemistry*, vol. 43, p. 582-584, DOI:10.1134/S1087659617060153.
- [12] Shevchenko, V.Ya., Sychev, M.M., Lapshin, A.E., Lebedev, L.A., Gruzdov, A.A., Glezer, A.M. (2017). Polymer structures with the topology of triply periodic minimal surfaces. *Glass Physics and Chemistry*, vol. 43, p. 608-610, DOI:10.1134/S1087659617060177.
- [13] Lord, E.A., Mackay, A.L., Ranganathan, S. (2006) *New Geometries for New Materials*. Cambridge University Press, Cambridge.
- [14] Sychov, M.M., Lebedev, L.A., Dyachenko, S.V., Nefedova, L.A. (2018). Mechanical properties of energy-absorbing structures with triply periodic minimal surface topology. *Acta Astronautica*, vol. 150, p. 81-84, DOI:10.1016/j.actaastro.2017.12.034.
- [15] Diachenko, S.V., Lebedev, L.A., Sychov, M.M., Nefedova, L.A. (2018). Physicomechanical properties of a model material in the form of a cube with the topology of triply periodic minimal surfaces of the gyroid type. *Technical Physics*, vol. 63, p. 984-987, DOI:10.1134/S1063784218070101.
- [16] Balabanov, S.V., Makogon, A.I., Sychev, M.M., Evstratov, A.A., Regazzi, A., Lopez-Cuest, J.M. (2020) 3D printing and mechanical properties of polyamide products with Schwartz primitive topology. *Technical Physics*, vol. 65, p. 211-215, DOI:10.1134/S1063784220020036.
- [17] Arsentev, M.Y., Balabanov, S.V., Makogon, A.I., Sychev, M.M. (2019). Experimental and theoretical studies of the mechanical properties of 3D printed polyamide products of the Schwarz primitive topology. *Glass Physics and Chemistry*, vol. 45, p. 599-602, DOI:10.1134/S1087659619060026.
- [18] Balabanov, S.V., Makogon, A.I., Sychov, M.M., Gravit, M.V., Kurakin, M.K. (2020). Mechanical properties of 3D printed cellular structures with topology of triply periodic minimal surfaces. *Materials Today: Proceedings*, vol. 30, p. 439-442, DOI:10.1016/j.matpr.2019.12.392.
- [19] Yoo, D.J. (2014). Recent trends and challenges in computer-aided design of additive manufacturing-based biomimetic scaffolds and bioartificial organs. *International Journal of Precision Engineering and Manufacturing*, vol. 15, p. 2205-2217, DOI:10.1007/s12541-014-0583-7.
- [20] Al-Ketan, O., Rowshan, R., Abu Al-Rub, R.K. (2018). Topology-mechanical property relationship of 3D printed strut, skeletal, and sheet based periodic metallic cellular materials. *Additive Manufacturing*, vol. 19, p. 167-183, DOI:10.1016/j.addma.2017.12.006.
- [21] Lin, Z.-H., Pan, J.-H., Li, H.-Y. (2022) Mechanical strength of triply periodic minimal surface lattices subjected to three-point bending. *Polymers*, vol. 14, no. 14, 2885, DOI:10.3390/polym14142885.
- [22] Arsentev, M.Yu., Sysoev, E.I., Makogon, A.I., Balabanov, S.V., Sychev, M.M., Hammouri, M.H., Vyacheslav A. Moshnikov, V.A. (2023). High-throughput screening of 3D-printed architected materials inspired by crystal lattices: procedure, challenges, and mechanical properties. *ACS Omega*, vol. 8, no. 28, p. 24865-24874, DOI:10.1021/acsomega.3c00874.
- [23] Zhu, L.Y., Li, L., Li, Z.A., Shi, J.P., Tang, W.I., Yang, J.Q., Jiang, Q. (2019) Design and biomechanical characteristics of porous meniscal implant structures using triply periodic minimal surfaces. *Journal of Translational Medicine*, vol. 17, 89, DOI:10.1186/s12967-019-1834-2.
- [24] GOST 11262-2017 (ISO 527-2:2012) *Plastics. Tensile test method*. JSC «Institute of plastics». Moscow. (in Russian).
- [25] GOST 4648-2014 (ISO 178:2010). *Plastics. Static bending test method*. JSC «Institute of plastics». Moscow. (in Russian).
- [26] GOST 4651-2014 (ISO 604:2002). *Plastics. Compression test method*. JSC «Institute of plastics». Moscow. (in Russian).
- [27] Han, J., Cao, Z., Gao, W. (2013). Remarkable sorption properties of polyamide 12 microspheres for a broad-spectrum antibacterial (triclosan) in water. *Journal of Materials Chemistry A*, no. 16, p. 4941-4944, DOI:10.1039/c3ta00090g.
- [28] Ma, N., Liu, W., Ma, L., He, S., Liu, H., Zhang, Z., Sun, A., Huang, M., Chengshen Zhu, C. (2020). Crystal transition and thermal behavior of Nylon 12. *e-Polymers*, vol. 20, no. 1, p. 346-352, DOI:10.1515/epoly-2020-0039.
- [29] GOST R 55135-2012 (ISO 11357-2:1999). *Plastics. Differential scanning calorimetry (DSC). Part 2. Determination of the glass transition temperature*. JSC «Institute of plastics». Moscow. (in Russian).
- [30] GOST R 57931-2017. *Polymer composites. Determination of the melting and crystallization temperature by thermal analysis methods*. FSUC «VIAM». Moscow. (in Russian).
- [31] Craft, G.M. (2018). *Characterization of Nylon-12 in a novel additive manufacturing technology, and the rheological and spectroscopic analysis of PEG-starch matrix interactions*. PhD thesis, University of South Florida, Tampa.
- [32] ANID. Polyamide - 12. from <https://anid.su/product/poliamid/poliamid-12>, accessed on 2022-02-22. (In Russian)
- [33] GOST 4670-2015. *Plastics. Determination of hardness. The method of pressing the ball*. JSC «Institute of plastics». Moscow. (in Russian).
- [34] GOST 24621-2015 (ISO 868:2003). *Plastics and ebonite. Determination of indentation hardness using a durometer (Shore hardness)*. JSC «Institute of plastics». Moscow. (in Russian).
- [35] GOST 15173-70. *Plastics. A method for determining the average coefficient of linear thermal expansion*. USSR state committee on standards. Moscow. (in Russian).
- [36] GOST 2789-73. *Surface roughness. Parameters and characteristics*. USSR state committee on standards. Moscow. (in Russian).
- [37] Von Schnering, H.G., Nesper, R. (1991). Nodal surfaces of Fourier series: Fundamental invariants of structured matter. *Zeitschrift für Physik B Condensed Matter*, vol. 83, p. 407-412, DOI:10.1007/BF01313411.
- [38] Gross, B.C., Erkal, J.L., Lockwood, S.Y., Chen, C., Spence, D.M. (2014) Evaluation of 3D printing and its potential impact on biotechnology and the chemical sciences. *Analytical Chemistry*, vol. 86, no. 7, p. 3240-3253, DOI:10.1021/ac403397r.
- [39] Diachenko, S.V., Balabanov S.V., Kiryanov N.V., Litosov G.E., Nefedova L.A., Sychov M.M. (2023). Glass filled polyamide-12

applications in energy absorbing structures. *XIII Scientific and Technical Conference of Students*, p. 382. (in Russian)

[40] Gibson, L.J., Ashby, M.F. (1982). The mechanics of three-dimensional cellular materials. *Proceedings of the Royal Society of London: A*, vol. 382, p. 43-59, DOI:10.1098/rspa.1982.0088.